Optics & Laser Technology 139 (2021) 106948

Contents lists available at ScienceDirect

Optics and Laser Technology

journal homepage: www.elsevier.com/locate/optlastec

Full length article

Asymmetric oxide apertures of vertical-cavity surface-emitting lasers fabricated by unsymmetrical wet oxidation and its polarization control

Jiye Zhang [a,b], Jianwei Zhang [a,*], Xing Zhang [a], Yinli Zhou [a], Youwen Huang [a], Yongqiang Ning [a], Hongbo Zhu [a], Jun Zhang [a], Yugang Zeng [a], Lijun Wang [a]

[a] State Key Laboratory of Luminescence and Applications, Changchun Institute of Optics, Fine Mechanics and Physics, Chinese Academy of Sciences, Changchun 130033, China

[b] Center of Materials Science and Optoelectronics Engineering, University of Chinese Academy of Sciences, Beijing 100049, China

ARTICLE INFO

Keywords:
VCSEL
Anisotropy oxide apertures
Polarization control
Wet oxidation

ABSTRACT

Given the high symmetry of vertical-cavity surface-emitting lasers (VCSELs) along their emission axis, these lasers demonstrate intrinsic polarization instability. In this study, we report the anisotropy oxide apertures of VCSEL formed by the unsymmetrical airflow distribution during the wet oxidation process. The polarization directions of VCSELs with anisotropy oxide apertures are well-controlled. VCSELs with oxide apertures of 2 μm × 4.6 μm achieve an orthogonal polarization suppression ratio of more than 20 dB and side-mode suppression ratio of more than 25 dB. In addition, an asymmetric far field distribution is observed, which can be ascribed to the asymmetric oxide apertures.

1. Introduction

Vertical-cavity surface-emitting lasers (VCSELs) are used as the key source of datacom and sensor applications due to their low threshold, high speed, and vertical lasing [1–3]. Oxide-confined GaAs/AlGaAs-based structures are broadly used because of their low-cost production [4,5]. However, the light polarization of VCSELs is inherently unstable [6,7]. Even the polarization orientation of a single-mode VCSEL is not well-defined. As the injection current exceeds the threshold, the polarization randomly switches between two orthogonal directions [8,9] because the oscillation cavity and gain medium are isotropic [10].

The polarization stability of VCSELs is important for single-mode devices used in optical communications and optical sensing [11,12]. Numerous methods were proposed to achieve the polarization stability of VCSELs. The anisotropy loss obtained using anisotropic mesa shapes, such as a rectangular post, is widely reported [13]. The polarization mode can also be stabilized by growing VCSELs on off-angled substrates, growing asymmetric nanostructures in active layers, and introducing photonic layers into oscillation cavities [14]. Recently, stable polarization control is achieved through high-contrast sub-wavelength gratings on the topmost layer of VCSELs [15]. VCSELs with stable polarization emission at various wavelengths are widely studied and commercialized [16–18]. Such lasers with an operating wavelength of 890 nm are extensively used in microscale atomic clocks [19,20].

In this study, we investigate the fabrication of anisotropy oxide apertures of VCSELs through unsymmetrical airflow distribution within the oxidation furnace. This method clearly defines the polarization direction of VCSELs. VCSELs with an oxide aperture of 2 μm × 4.6 μm gain an orthogonal polarization suppression ratio (OPSR) of more than 20 dB and side-mode suppression ratio (SMSR) of more than 30 dB. When the oxide aperture increases to 5 μm × 8.5 μm, the OPSR of the VCSEL is reduced to approximately 15 dB, but the optical polarization remains stable. The divergence angles along two orthogonal directions are 12.4° and 6.9°; such a discrepancy is mainly caused by the asymmetrical optical apertures. The simulation model of anisotropy oxide aperture is built, and the unsymmetrical optical divergence is demonstrated in theory.

2. Model presentation

In our experiment, the top-emitting device structures are grown on n-type GaAs substrates through metal–organic chemical vapor deposition (MOCVD). The n-type distributed Bragg reflector (n-DBR) consists of 32 pairs of Si-doped $Al_{0.12}GaAs$ and $Al_{0.9}GaAs$ layers. A lambda optical cavity and C-doped 22-period top $Al_{0.12}GaAs/Al_{0.9}GaAs$ DBR are then grown on the n-DBR. The optical cavity consists of three compressively

* Corresponding author.
E-mail address: zjw1985@ciomp.ac.cn (J. Zhang).

https://doi.org/10.1016/j.optlastec.2021.106948
Received 9 June 2020; Received in revised form 27 December 2020; Accepted 16 January 2021
Available online 6 February 2021

strained 5 nm-thick $In_yGa_{1-y}As$ quantum wells and 8 nm-thick $Al_{0.3}Ga_{0.7}As$ barriers. For the selective oxidation, the 70 nm AlAs layer is used as the oxide layer because of the high anisotropic oxidation [21].

Fig. 1 shows the schematic of a GaAs/AlGaAs VCSEL. The presented model of the oxide aperture is used for the optical divergence simulation. The 3D finite-difference time-domain (FDTD) method is adopted to simulate the optical waveguide of different oxide apertures. During the simulation, a dipole source is set at the center of the oxide apertures. The outer boundary is set as a perfect matched layer (PML). The angular dependence of the oxidation rates of the thin AlAs layer grown in different substrate orientations is measured [21]. The finding reveals high oxidation rates for the $\langle \bar{1}10 \rangle$ direction. Therefore, the lengths of the two axes for the oxide aperture along the $\langle \bar{1}10 \rangle$ and $\langle 110 \rangle$ crystallographic directions, namely the x and y axial directions, respectively, are different (inset of Fig. 1).

3. Experiment setup

The epitaxial structure of 890 nm VCSEL was grown on a (100)-oriented GaAs substrate via MOCVD. The cylindrical mesa was lithographically defined and subsequently etched down to the n-DBR through inductively coupled plasma. The AlAs layer in the p-type DBR (p-DBR) was then exposed and oxidized in an N_2/H_2O atmosphere at elevated temperatures of nearly 410 °C. The anisotropic flow direction of the N_2/H_2O mixture gas was controlled along the two axes in the oxidation chamber by increasing the exhaust pump [22] to enhance the anisotropic oxidation of the AlAs layer. During the oxidation process, the $\langle 110 \rangle$ direction of the wafer was perpendicular to the gas flow direction, and the oxidation rate along this crystal direction was slow [23].

To obtain the accurate dimension of the oxide aperture, the p-DBR layers were etched away using H_2SO_4 and H_2O_2 solutions after the oxidation process [24]. Fig. 2 illustrates the evolution of the oxidation depth along two axes. The mesa diameter of the VCSEL is 30 μm. The lengths along the y and x axes of the oxide aperture are denoted as D_S and D_L, respectively. As the oxidation time increases from 8 min to 12 min, D_S decreases from 9.87 μm to 2 μm. The oxidation rate of the AlAs layer along the short axis is approximately 1.25 μm/min.

The difference in the oxidation depth along the two axes is not obvious until the oxidation time reaches 10 min. The difference between the two axial directions of the oxidation apertures rapidly increases when the oxidation time exceeds 10 min. When the oxidation time reaches 12 min, the oxidation depth difference between the two axial directions decreases. This decline can be ascribed to the inhibited oxidation reaction along the $\langle \bar{1}10 \rangle$ direction due to the high-density AlO_x production [25], which prevents the penetration of the N_2/H_2O mixture gas when the oxidation depth exceeds 14 μm. The oxidation

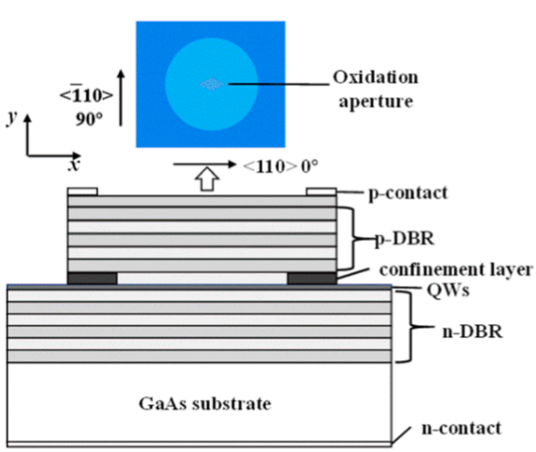

Fig. 1. Cross-sectional schematic of the VCSEL structure. The inset image denotes the oxide aperture model with a diamond shape, which is built via FDTD.

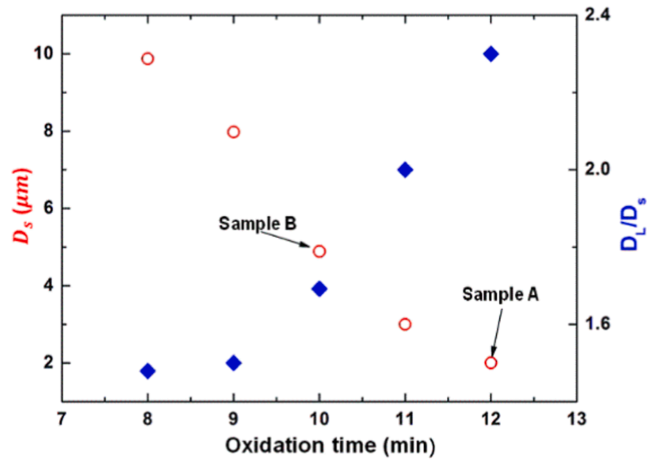

Fig. 2. Evolution of the oxidation depth along the $\langle 110 \rangle$ and $\langle \bar{1}10 \rangle$ directions. The diameter of the mesa is 30 μm. The inset figures are the oxide aperture formed with an oxidation time of 10 min.

time in this study is set to 10 and 12 min. The dimensions of the oxide apertures along the y axial direction are 5 and 2 μm, respectively. The VCSEL with 2 μm oxide aperture along the y-axis is called sample A, whereas the other sample is called sample B.

4. Results and discussion

Fig. 3 shows the setup for measuring the optical power and far field of the examined VCSEL. The VCSEL chip is packaged on the TO-46, and the operating temperature of the laser is maintained at 25 °C by the thermoelectric cooler controller. The model of the linear polarizer used in the experiment is Thorlabs LPVIS050. To characterize the polarization directions, we measured the optical power along the different angles in the plane of VCSEL by rotating the linear polarizer. The polarization ratio of the output power is determined by rotating the polarizer so that its orientation is orthogonal and parallel to the major polarization direction of VCSEL.

The optical power of sample A along different polarization angles is depicted in Fig. 4. The inset figure shows the near-field pattern near the threshold. The shuttle-shaped pattern is also observed. The optical power of sample A changes with the rotating angle of the polarizer, which represents the polarization direction. The maximum optical power appears at the x-axis of the oxide aperture, whereas the minimum optical power is observed in the y-axis. Therefore, the linearly polarized light is obtained by the shuttle shaped oxide aperture. The OPSR represents the degree of polarization, which is the ratio of the optical power along the main polarization and its orthogonal directions. This ratio can be calculated as OPSR = $10 \times \log(P_{max}/P_{min})$. As shown in Fig. 4, the optical power is observed in other polarization angles, except for the main polarization and its orthogonal direction. They represent the different components of major polarization according to Malus' law.

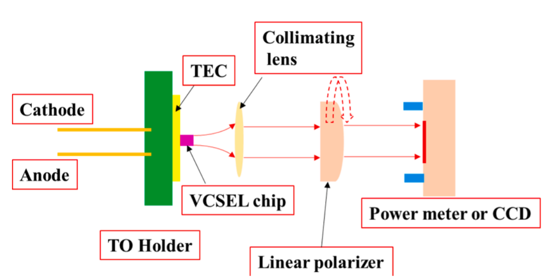

Fig. 3. Experimental setup for measuring the optical power and far field along the different polarization directions of VCSEL.

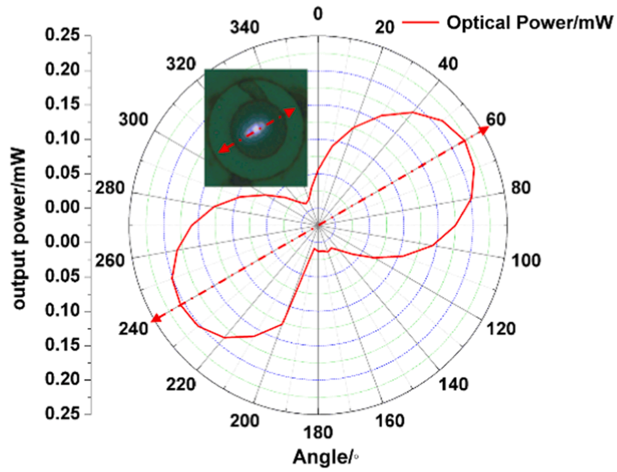

Fig. 4. Optical power of sample A in different polarization angles. The inset figure depicts the corresponding near-field. The angle that corresponds to the long axis of the oxide aperture is marked by the arrow.

Fig. 5 depicts the polarization-resolved light–current characteristics of samples A and B. The light–current curves respectively indicate the optical powers measured behind a linear polarizer whose transmission direction is oriented parallel and orthogonal to the x axial polarization direction of VCSEL. These optical powers are called the major and minor powers, respectively.

As shown in Fig. 5, the polarization directions of the two samples remain stable from the threshold current to the thermal saturation point. The OPSR–current curves of the two samples are also shown in Fig. 5. The OPSR is calculated from the light–current data of currents with steps of 0.1 mA. The device of sample A maintains a stable polarization up to the thermal saturation point, and the maximum magnitude of the OPSR is 22 dB. The output power and threshold current of sample B are higher than those of sample A due to its larger oxide aperture. In addition, the former displays a stable polarization and obtains an OPSR of more than 15 dB within the operating current range of 1.5–6 mA.

Fig. 6 shows the polarization-resolved spectra of samples A and B at an operating current of 6 mA. The dominant polarizations of both VCSELs are stable, which is consistent with the behavior of the OPSR curve in Fig. 5. Sample A exhibits a single-mode operation with an SMSR

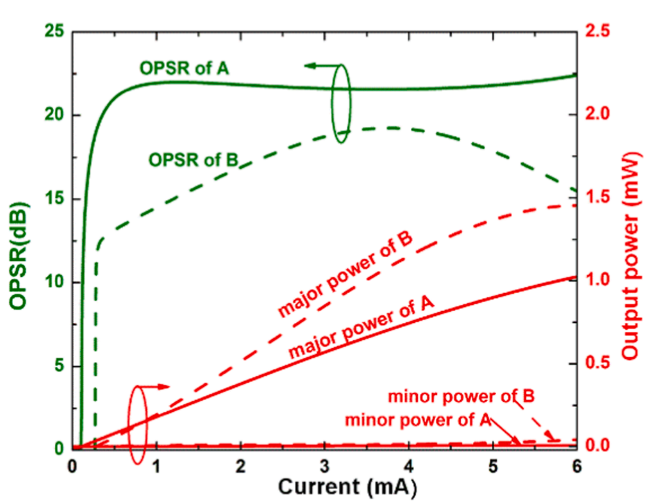

Fig. 5. Polarization-resolved light–current curves of samples A and B under continuous-wave operation. The change in the OPSR with the operating current is also presented. The optical power in the major polarization direction is called the major power, whereas the optical power orthogonal to the major polarization direction is called the minor power.

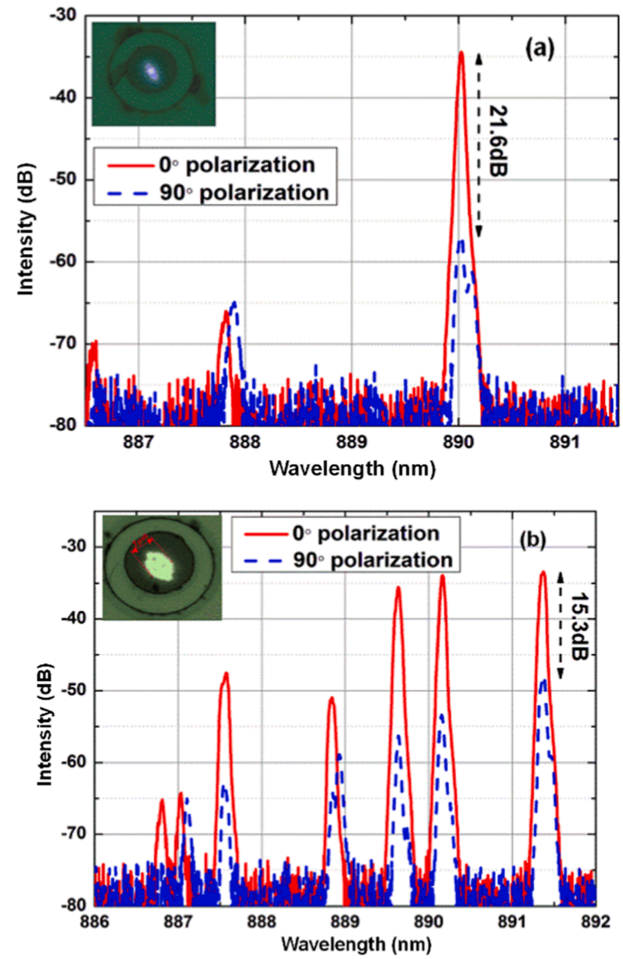

Fig. 6. Polarization-resolved spectra of samples (a) A and (b) B. The inset figures are the near fields of both samples near the threshold. The figure also presents the anisotropy profiles of the near fields.

of nearly 30 dB. The peak-to-peak difference between the dominant and suppressed polarization modes is 21.6 dB. The spectrum of sample B indicates a highly multimodal operation, and the peak-to-peak difference between the dominant and suppressed polarization modes of this sample is 15.3 dB. The inset figures show the near-fields of samples A and B near the threshold. Both samples display unsymmetrical near-field patterns. This phenomenon represents the anisotropy oxide apertures. The length of the near field of sample B along the short axis is nearly 7 μm. Therefore, the multimode operation of this sample can be attributed to the large dimension of its oxide aperture.

Fig. 7 shows the far fields that are parallel and orthogonal to the x axial polarization direction. These profiles are respectively denoted as the major and minor axes of sample A. The cross-section profiles are extracted and plotted against the divergence angle. A full divergence angle at full width at half maximum (FWHM) of 8.2° is observed in the major axis, whereas an FWHM of 4.8° appears in the minor axis. The presence of side lobes in the emission far-fields proves that VCSELs with anisotropy oxide apertures might suffer from diffraction losses in air. As shown in the inset of Fig. 7(a), the different far-field patterns along the two axial directions indicate an asymmetrical beam profile.

The FDTD method is used to simulate the far field of a VCSEL with shuttle-shaped oxide aperture, which is identical to the oxide aperture of sample A. The simulation results are presented in Fig. 7(b). An elliptical far-field pattern is obtained, which is similar to the far field of sample A (Fig. 7(a)). Moreover, the far-field profiles along the major and minor axes are different from each other. A dipole light source is used, and the outer boundary is set as a PML without light scattering. No side lobes are

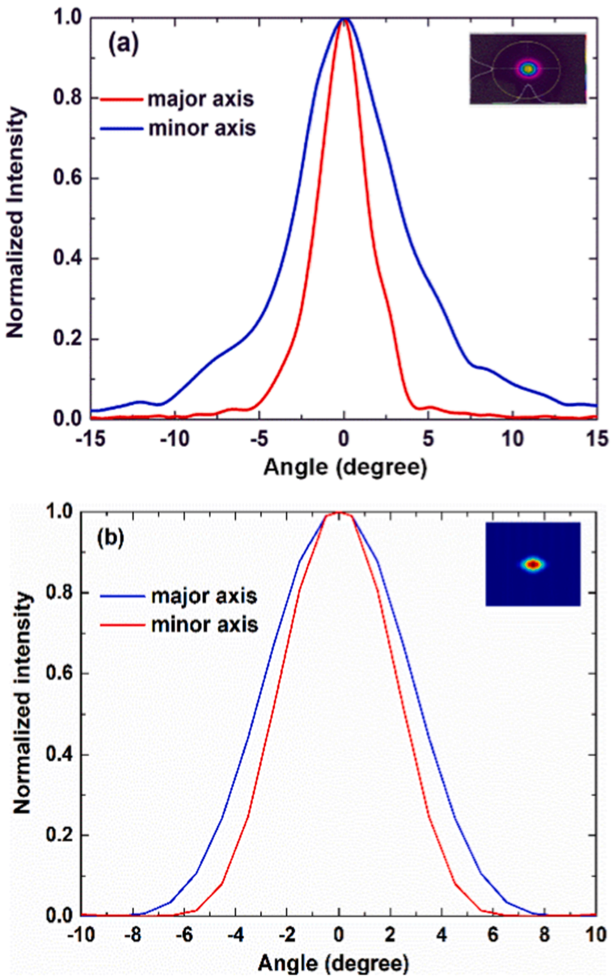

Fig. 7. (a) Far-field profiles that are parallel and orthogonal to the direction of the dominant polarization of sample A at a driving current of 6 mA and (b) the calculated far-field profile of sample A. The inset figures are the 2D views of the far-field patterns.

present in the emission far-fields, and the Gaussian-like shape reflects the single-mode emission of the shuttle-shaped oxide aperture.

The results suggest that increasing the length difference of the two axes of the oxide aperture is beneficial in realizing the polarization stability of VCSELs. The reason for this inference is because strain and stress are introduced during the epitaxial growth of the VCSEL structure, thereby generating slight birefringence. This phenomenon causes the resonance cavity of devices to operate under two transverse electric/transverse magnetic (TE/TM) modes with similar gain but slightly different frequencies at two axial polarization directions. However, different numbers of electric dipoles in the two TE/TM modes are generated at the edge of the asymmetric oxide aperture, and thus lead to unequal scattering loss [26]. The electric field E introduced by the electric dipoles decays exponentially at the radial direction. Therefore, the electric dipole moment P of the dipole can be expressed as

$$P = e \times r \times E(r) = e \times r \times \exp\left(-\frac{r^2}{\omega^2}\right), \tag{1}$$

where e is the amount of electron charge, r is the distance from the edge to the center of the oxide aperture, and ω is the waist beam radius of light. Formula (1) can be used to derive the value of r.

$$\frac{\partial P}{\partial r} = e \times \exp\left(-\frac{r^2}{\omega^2}\right) \times \left(1 - \frac{r^2}{\omega^2}\right) \tag{2}$$

where e and the exponential function are always greater than 0, and ω is less than r. Consequently, P decreases with the increase in r. In an asymmetric oxide aperture, the electric dipole moment $P(D_L/2)$ is smaller than $P(Ds/2)$. The above calculation shows that the scattering loss along the long axis of the oxide aperture is always smaller than that along the short axis. Given that scattering losses dominate the total cavity losses for aperture sizes [27,28], the difference in such losses between the two axial polarization directions is sufficient to select the mode, and thus leads to polarization pinning.

5. Conclusions

In this study, we experimentally demonstrate the shuttle-shaped oxide aperture for the polarization control of VCSEL by adopting the unsymmetrical airflow distribution during the wet oxidation process. The results indicate that the single-mode and single-polarization operation of VCSELs can be achieved using this oxide aperture. In addition, OPSR and SMSR of more than 20 and 30 dB, respectively, are gained. However, an asymmetrical beam profile caused by the shuttle-shaped oxide aperture is observed. This drawback can be improved by using small size difference along the two orthogonal directions.

Declaration of Competing Interest

The authors declare no conflict of interest.

Acknowledgement

This work is supported by the National Key Research and Development Program of China (No. 2018YFB2002401), National Natural Science Foundation of China (Nos. 61874117, 11674314, 11774343, and 61727822), Equipment Advanced Research Fund (No. 61404140107), and Key Projects of Jilin Province Science and Technology Development Plan (No. 20180201119GX).

References

[1] F. Koyama, Advances and new functions of VCSEL photonics, Opt. Rev. 21 (6) (2014) 893–904.

[2] D. Bimberg, Ultrafast VCSELs for datacom, IEEE Photonics J. 2 (2) (2010) 273–275.

[3] K. Gulden, Y. Gao, P. Royo, M. Brunner, Commercialization of VCSELs and VCSEL arrays, Proc. SPIE 5280 (2004) 506–515.

[4] K. Iga, Surface-emitting laser-its birth and generation of new optoelectronics field, IEEE J. Sel. Top. Quantum Electron. 6 (6) (2000) 1201–1215.

[5] D. Inoue, R. Kubota, T. Aoki, T. Ishizuka, M. Yanagisawa, H. Shoji, 1×4 VCSEL arrays with uniform spectral and noise properties by using rotationally asymmetric oxide aperture for 400 Gbit/s applications, Proc. SPIE 11300 (113000F) (2020).

[6] A. Larsson, Advances in VCSELs for communication and sensing, IEEE J. Sel. Top. Quantum Electron. 17 (6) (2011) 1–16.

[7] M.J. Miah, A. Al-Samaneh, A. Kern, D. Wahl, P. Debernardi, R. Michalzik, Fabrication and characterization of low threshold polarization-stable VCSELs for Cs-based miniaturized atomic clocks, IEEE J. Sel. Top. Quantum Electron. 19 (4) (2013) 1–10.

[8] S.H. Lee, H.W. Jung, K.H. Kim, M.H. Lee, All-optical flip-flop operation based on polarization bistability of conventional-type 1.55-μm wavelength single-mode VCSELs, J. Opt. Soc. Korea 14 (2) (2010) 137–141.

[9] J.M. Ostermann, F. Rinaldi, P. Debernardi, R. Michalzik, VCSELs with enhanced single-mode power and stabilized polarization for oxygen sensing, IEEE Photonics Technol. Lett. 17 (11) (2005) 2256–2258.

[10] S. Calvez, G. Lafleur, A. Arnoult, Antoine Monmayrant, Henri Camon, G. Almuneau, Modelling anisotropic lateral oxidation from circular mesas, Opt. Mater. Express 8 (7) (2018) 1762–1773.

[11] R. Michalzik, J.M. Ostermann, P. Debernardi, Polarization-stable monolithic VCSELs, Proc. SPIE 6908 (2008) 69080A.1–69080A.16.

[12] Y. Hong, J. Paul, P.S. Spencer, K.A. Shore, The effects of polarization-resolved optical feedback on the relative intensity noise and polarization stability of vertical-cavity surface-emitting lasers, J. Lightwave Technol. 24 (8) (2006) 3210–3216.

[13] T. Yoshikawa, T. Kawakami, Polarization-controlled single-mode VCSEL, IEEE J. Quantum Electron. 34 (6) (1998) 1009–1015.

[14] K. Fumio, P.B. Dayal, A review on polarization control of vertical-cavity surface-emitting semiconductor lasers, Recent Patents Electr. Electron. Eng. 4 (2) (2011) 81–97.

[15] Y. Tsunemi, K. Ikeda, H. Kawaguchi, Lasing-polarization-dependent output from orthogonal waveguides in high-index-contrast subwavelength grating vertical-

cavity surface-emitting laser, Appl. Phys. Express 6 (9) (2013), 092106.1–092106.4.
[16] X. Zhang, B. Liu, K. Shi, F. Han, H. Chen, L. Nie, X. Yu, A thermal analysis of stable-polarization VCSELs, Optik 157 (2018) 203–207.
[17] T. Katayama, K. Nakao, D. Hayashi, Hitoshi Kawaguchi, Flip-flops using polarization bistable VCSEL with and-gate functionality by two wavelength inputs, Ieice Electron. Express 13 (5) (2016) 20160064.
[18] X. Zhang, Y. Chen, Q. Ma, et al., A beam-shaped study of the stable polarization VCSEL, Appl. Phys. Lett. 125 (6) (2019), 97.1–97.5.
[19] A. Al-Samaneh, M. Bou Sanayeh, M.J. Miah, W. Schwarz, D. Wahl, A. Kern, R. Michalzik, Polarization-stable vertical-cavity surface-emitting lasers with inverted grating relief for use in microscale atomic clocks, Appl. Phys. Lett. 101 (17) (2011) 1–4.
[20] Jianwei Zhang, Xing Zhang, Hongbo Zhu, Jian Zhang, Yongqiang Ning, Li Qin, Lijun Wang, High-temperature operating 894.6nm-VCSELs with extremely low threshold for Cs-based chip scale atomic clocks, Opt. Express 23 (11) (2015) 14763.
[21] P.O. Vaccaro, K. Koizumi, K. Fujita, T. Ohachi, AlAs oxidation process in GaAs/AlGaAs/AlAs heterostructures grown by molecular beam epitaxy on GaAs (n11) A substrates, Microelectron. J. 30 (4/5) (1999) 387–391.
[22] W. Nakwaski, M. Wasiak, P. Mackowiak, W. Bedyk, M. Osiński, A. Passaseo, V. Tasco, M.T. Todaro, M.D. Vittorio, R. Joray, J.X. Chen, R.P. Stanley, A. Fiore, Oxidation kinetics of AlAs and (AlGa)As layers in GaAs-based diode laser structures: comparative analysis of available experimental data, Semicond. Sci. Technol. 19 (3) (2004) 333–341.
[23] G. Lafleur, G. Almuneau, A. Arnoult, H. Camon, S. Calvez, Anisotropy in the wet thermal oxidation o fAlGaAs: influence of process parameters, Opt. Mater. Express 8 (7) (2018) 1788–1795.
[24] W.S. Lau, E.F. Chor, S.P. Kek, W.H.B. Abdul Aziz, H.C. Lim, C.H. Heng, R. Zhao, The development of a highly selective KI/I2/H2O/H2SO4 etchant for the selective etching of Al0.3Ga0.7As over GaAs, Jap. J. Appl. Phys. 36 (6) (1997) 3770–3774.
[25] F. Chouchane, G. Almuneau, O. Gauthier-Lafaye, A. Monmayrant, A. Arnoult, G. Lacoste, C. Fontaine, Observation of overstrain in the coalescence zone of AlAs/AlOx oxidation fronts, Appl. Phys. Lett. 98 (26) (2011), 261921.1–261921.3.
[26] E. Nhan, S. Riyopoulos, Interpretation of polarization pinning due to scattering loss differentiation in asymmetric vertical -cavity surface emitting laser cavities, Jap. J. Appl. Phys. 99 (12) (2006), 123101-1—123101-7.
[27] T. Yoshikawa, T. Kawakami, H. Saito, H. Kosaka, M. Kajita, K. Kurihara, Y. Sugimoto, K. Kasahara, Polarization-controlled single-mode VCSEL, IEEE J. Quantum Electron. 34 (6) (1998) 1009–1015.
[28] A. Bond, P.D. Dapkus, J.D. O`Brien, Design of low-loss single-mode vertical-cavity surface-emitting lasers, IEEE J. Sel. Top. Quantum Electron. 5 (3) (2002) 574–581.